

Intricacies of Frustrated Magnetism in the Kondo Metal YbAgGe

D. G. Mazzone,^{1,*} C. B. Larsen,¹ B. Ueland,^{2,3} X. Boraley,¹ D. M. Pajerowski,⁴ Y. Skourski,⁵ J. Taylor,⁶ B. Fåk,⁷ S. L. Bud'ko,^{2,3} R. McQueeney,^{2,3} P. C. Canfield,^{2,3} and O. Zaharko^{1,†}

¹PSI Center for Neutron and Muon Sciences, 5232 Villigen PSI, Switzerland

²Department of Physics and Astronomy, Iowa State University, Ames, Iowa 50011, USA

³Ames National Laboratory, Iowa State University, Ames, Iowa 50011, USA

⁴Neutron Scattering Division, Oak Ridge National Laboratory, Oak Ridge, Tennessee 37831, USA

⁵Dresden High Magnetic Field Laboratory (HLD-EMFL),

Helmholtz-Zentrum Dresden-Rossendorf, 01328 Dresden, Germany

⁶ISIS Facility, STFC Rutherford Appleton Laboratory,

Harwell Science and Innovation Campus, Oxfordshire OX11 0QX, United Kingdom

⁷Institut Laue-Langevin, 71 Avenue des Martyrs, CS20156, 38042 Grenoble Cédex 9, France

(Dated: September 3, 2025)

The combination of localized magnetic moments, their frustration and interaction with itinerant electrons is a key challenge of condensed matter physics. Frustrated magnetic interactions promote degenerate ground states with enhanced fluctuations, a topic that is predominantly studied in magnetic insulators. The coupling between itinerant and localized electrons in metals add complexity to the problem, and presently formulated only for extreme cases in which the itinerant electrons mediate exchange between localized spins (RKKY interaction) or suppress the formation of magnetic moments (Kondo screening). Here, we report an in-depth experimental study of the distorted Kagome metal YbAgGe, unravelling the open questions of how frustration, localized magnetism and itinerant electrons are intertwined in frustrated Kondo metals. We find that coupled itinerant and localized electrons give rise to dynamic magnetic correlations below $T^* \approx 20$ K. At lower temperature, frustrated magnetic interactions establish anisotropic magnetic short-range correlations that culminate into antiferromagnetic long-range order below $T_N = 0.68$ K with a significantly reduced modulated magnetic moment. We show that local moment Hamiltonians can yield limited understanding of the microscopic behaviour in frustrated metals, and prompt the extension of more sophisticated model Hamiltonians incorporating itinerant effects.

Introduction

Magnetic frustration in materials arises from constraints of the underlying lattice geometry or conflicting exchange interactions, which can yield degenerate magnetic configurations with unusual ground states such as skyrmion lattices¹, spin glasses², spin liquids³ and other phases that may be attractive for future technological applications. A microscopic understanding of these frustrated magnetic states is often achieved through local-moment magnetic Hamiltonians with nearest-neighbour spin interactions^{4,5}. These microscopic models have

proven fruitful for insulating materials in which itinerant electrons can be neglected, further neighbour interactions decay promptly with distance, and higher-order spin interactions are strongly suppressed⁶. The approach is less effective for magnetically frustrated metals. For this material class it is often necessary to account for long-range Fermi surface effects, in which conduction electrons interact with the local moments of the magnetic ions.

Microscopic Hamiltonians appropriate for magnetic metals with embedded localized moments are derived from the Kondo lattice Hamiltonian (KLH) $H_{KLH} = H_{kin} + H_{ex}$ ^{6,7}. Here, H_{kin} describes the kinetic motion of the itinerant electrons, and H_{ex} represents the coupling of the localized spins with the conduction electrons. The KLH is particularly important for rare-earth compounds⁸, for which the relevant RKKY interaction^{9–11} can be derived as lowest-order contribution⁶. In this model the conduction electrons serve as exchange pathways between local magnetic moments, directly encoding the Fermi surface into local exchange parameters J of effective Heisenberg-like Hamiltonians. Within this approach, it is possible to treat magnetism in metals similarly to the insulating case, but with anisotropic exchanges interactions. This allows for the exploration of novel frustrated quantum phases in metals^{6,12–15}, though their interpretation often remains challenging.

Metals containing rare-earth ions such as Ce, Eu, Sm and Yb experience an additional interaction. The conduction electrons can (partially) screen localized moments, engaging them into collective singlet states¹⁶. This Kondo screening process can be understood through an extension of H_{ex} , encrypting an antiferromagnetic coupling between the localized f -electrons and the conduction bands¹⁷. The admixture between these electrons can become coherent at low temperature, leading to hybridized electron bands with heavy effective masses close to the Fermi surface. A microscopic band description of these heavy-fermion systems has proven to be notoriously challenging, as most *ab-initio* calculations have difficulties to distinguish the small energy differences of the various emergent states. Magnetic frustration com-

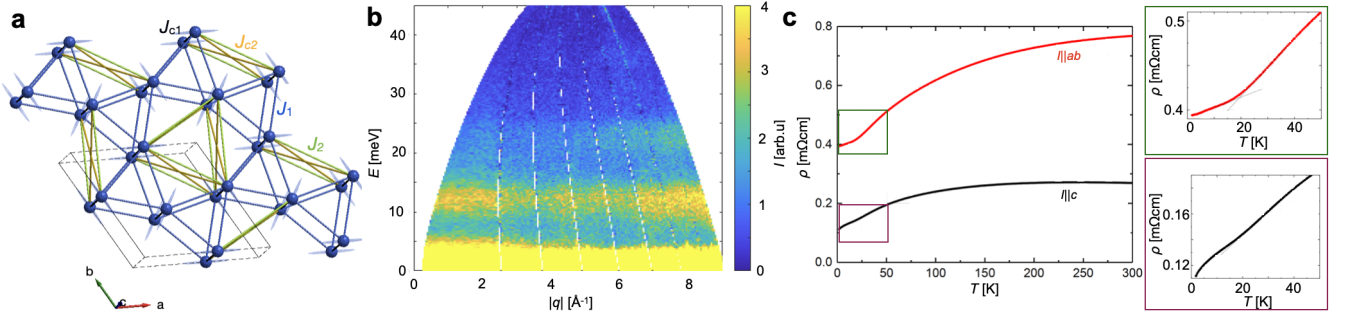


FIG. 1. **The three main ingredients in frustrated Kondo metals.** **a** *Frustration*: the Yb^{3+} ions in YbAgGe generate a distorted Kagome structure with nearest and next-nearest neighbour interactions J_1 (blue) and J_2 (green) in the hexagonal plane and nearest neighbour J_{c1} (black) and J_{c2} (gold) interplane interactions. Single ion anisotropy ellipsoids are shown in blue. **b** *Local magnetism*: inelastic neutron scattering data for energy transfers $E < 45$ meV and wavevector transfers $|q| < 9 \text{ \AA}^{-1}$ measured at $T = 3$ K on the MARI spectrometer. The transition at $E = 12$ meV originates from a CEF excitation mixed with a phonon, the transition at $E = 23$ meV is attributed to phononic contributions. **c** *Itinerant electrons*: electrical resistivity measurements in which the electric current I runs parallel or perpendicular to the crystallographic c -axis. Below $T^* = 20$ K additional scattering processes yield deviations from the temperature dependence at higher temperature.

plicates the matter, because theoretical predictions need to ascertain whether various spin configurations are degenerate or separated in energy. To this end, we address the question of how the three ingredients - RKKY interaction, Kondo screening and frustration - intertwine to establish the physics in YbAgGe .

Local Magnetism and Frustration

YbAgGe is a member of the RAgGe family crystallizing in the hexagonal ZrNiAl -type crystal structure (space group $P6_2/m$)¹⁸, in which Yb^{3+} ions form distorted Kagome layers with periodicity $a = b = 7.05 \text{ \AA}$ perpendicular to $c = 4.14 \text{ \AA}$ (see Fig. 1a and Supplementary Information (SI) Note 1 for details). Within the localized model the overarching magnetic energy scale is determined by the localized Yb^{3+} Kramers ions, with total angular momentum $J = 7/2$. The $2J+1 = 8$ degenerate eigenstates of the Yb^{3+} ion are split by the non-spherical crystal-electric field (CEF). The lowest CEF transition has at an energy transfer of $E = 12.0(4)$ meV, manifesting as a non-dispersing excitation in our polycrystalline inelastic neutron scattering (INS) experiment on the MARI spectrometer at ISIS (Fig. 1b). The transition is in agreement with earlier reports^{19,20}. Using PyCrystalField²¹ our calculation establishes that the ground state retains the axial anisotropy, aligned with 2-fold axes passing through the Yb^{3+} ions (see Fig. 1a) and predicts a magnetic moment of $\mu_{CEF} = 3.98\mu_B$ (see SI Note 2 for details).

Within the localized picture the Heisenberg exchange Hamiltonian approximation enables to predict effective magnetic models for the RAgGe crystal geometry. They range from Kagome spin layer models, when the frustration between intraplane interactions J_i prevails, to spin chain models, when the frustration is dominant within the interplane interactions J_{ci} . For instance, in the $R = \text{Tm}$ member the energy hierarchy can be resolved

as follows:²² i) the CEF-anisotropy dominates the magnetic exchange interactions; ii) the strongest magnetic exchange coupling J_c along the c -axis is ferromagnetic (FM) and not frustrated; iii) the interplay between weaker, intraplane J_1 , J_2 couplings manifests ice rules for the J_2 triangles, but the spin-ice frustration is released by the significant equidistant but distinct J_{3a} and J_{3b} terms (see also SI Note 3). In YbAgGe the CEF-anisotropy is the same as in TmAgGe , but its contribution is less strong. This allows for interplane interactions J_{ci} to gain in importance yielding frustration effects alongside the interplane couplings.

In fact according to macroscopic studies and neutron diffraction results²³ antiferromagnetic (AFM) long-range order (LRO) in YbAgGe is established below $T_N = 0.68$ K with a propagation vector of $q = (1/3, 0, 1/3)$. The order is unconventional, featuring varying moment sizes on different atoms with an average amplitude of $1.62(3)\mu_B/\text{Yb}$. A magnetic field applied in the Kagome plane triggers a series of metamagnetic transitions to other LRO states with different periodicity in the Kagome plane, but with persistent $q_z \approx 1/3$ component. Above $\mu_0 H \approx 7$ T ($H \parallel [1, -1, 0]$) these modulations vanish, so that eventually only an induced FM component remains (see SI Note 1 for details). We attempted to conceive the dominant exchange interactions in YbAgGe by minimizing the Heisenberg-type Hamiltonian and analyzing the solutions with the propagation vectors determined in earlier experiments²³ (see SI Note 3). We find that the $q = (1/3, 0, 1/3)$ propagation vector requires AFM nearest-neighbour interplane interactions J_{c1} and J_{c2} , and finite further neighbour intraplane terms J_3 .

Remarkably, YbAgGe exhibits increased magnetic correlations already above T_N , for $T < 2$ K²⁴. Figures 2a and b show single crystal elastic scattering maps, which we measured on the Cold Neutron Chopper Spectrome-

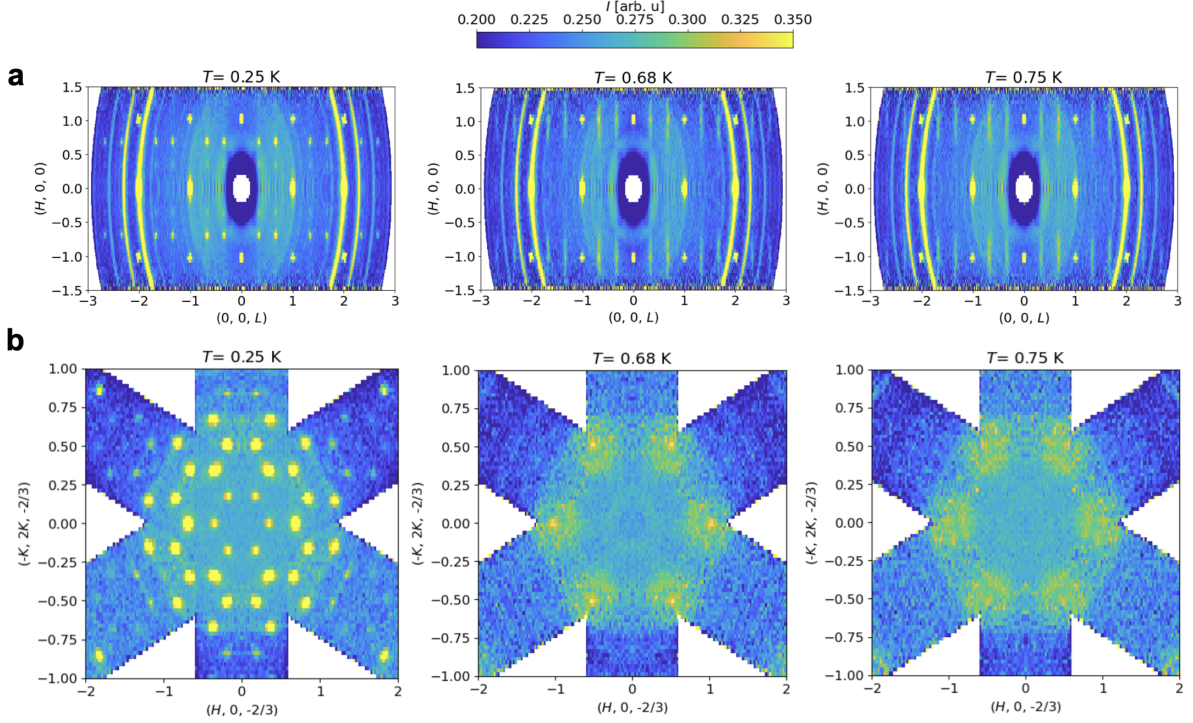


FIG. 2. **Static magnetism in YbAgGe.** Two dimensional reciprocal space maps in **a** the $(H, 0, L)$ plane and **b** perpendicular to $(0, 0, -2/3)$ measured at $T = 0.25, 0.68$ and 0.75 K. Below $T \approx 2$ K antiferromagnetic short-range correlations emerge at a wavevector $q = (0, 0, 1/3)$ with a correlation length along the c -axis which exceeds the in-plane correlation length by at least a factor of five. Below a first-order transition at $T = 0.68$ K long-range order is developed at $q = (1/3, 0, 1/3)$. Further detailed information is given in SI Note 3 and 4. The data were measured at the Cold Neutron Chopper Spectrometer (CNCS) using an incident energy of $E_i = 12$ meV. The figures were generated using an energy integration $\Delta E = [-1/2, 1/2]$ meV and a reciprocal space integration $\Delta Q = [-0.1, 0.1]$ and $[-0.69, -0.63]$ rlu perpendicular to the reciprocal plane in panel **a** and **b**, respectively.

ter (CNCS) at ORNL in the $(H, 0, L)$ and $(H, K, -2/3)$ planes for $T = 0.25, 0.68$ and 0.75 K. Upon cooling, diffuse scattering develops around $q = (0, 0, 1/3)$ positions, which is sharp along the L direction but broad along H . This corresponds to spin-spin correlations that are short-ranged within the hexagonal plane but extended along the c -axis (see SI Note 4 for details). We modeled the diffuse scattering as spin-spin correlations confined to a distorted-Kagome layer above $T = 0.68$ K and attempted to determine the dominant magnetic exchanges in the Kagome planes (see SI Note 3). The Fourier transform of simplistic moment arrangements with the local CEF anisotropy of Yb^{3+} ions and AFM J_1 and J_2 exchanges were calculated using Scatty²⁵ and are presented in Fig. S3.

Itinerant electrons

The metallic nature of the RAgGe family adds complexity to understanding the magnetism. The itinerant electrons affect the degeneracy of frustrated states, can lead to significant further neighbour exchange couplings and Kondo screening. We have collected a number of experimental evidences in YbAgGe , which do not comply with a localized moment picture. For instance, below $T^* \approx 20$ K, the temperature at which full $R\ln 2$ entropy is recovered^{24,26}, our electric resistivity measurements with

currents I parallel and perpendicular to the c -axis show deviations to the behaviour at high temperature (see Fig. 1c). These data, together with previous magnetization and specific heat results^{24,26} indicate a link between conduction electrons and local magnetic degrees of freedom, suggesting hybridization of Yb $4f$ electrons with the conduction bands. The magnetization measured at high magnetic fields is also incompatible with a localized picture (see SI Note 5). Another argument for itineracy is the reduced and amplitude modulated ordered magnetic moment value as determined from neutron diffraction. Even inside the AFM LRO state at zero field, the ordered moment is only $\mu_{\text{ord}} \approx 1.6\mu_B$ on average²³ implying a loss of $\sim 60\%$ when compared to the expected localized moment $\mu_{\text{CEF}} = 3.98\mu_B$.

The most striking counter to the localized picture is provided by our inelastic neutron scattering results. An analysis of the dipole-allowed transitions between the CEF ground state wavefunctions predicts the absence of observable magnetic excitations (see SI Note 2 for details). This is in strong contrast to our experimental findings shown in Fig. 3a measured at $T = 0.25$ K and $\mu_0 H = 0$ T on CNCS. We observe enhanced spectral weight along $(H, 0, 1/3)$, $(H, 0, 2/3)$ and around $(0, 0, 1/2)$. The intensity is modulated mainly along the c -axis, but

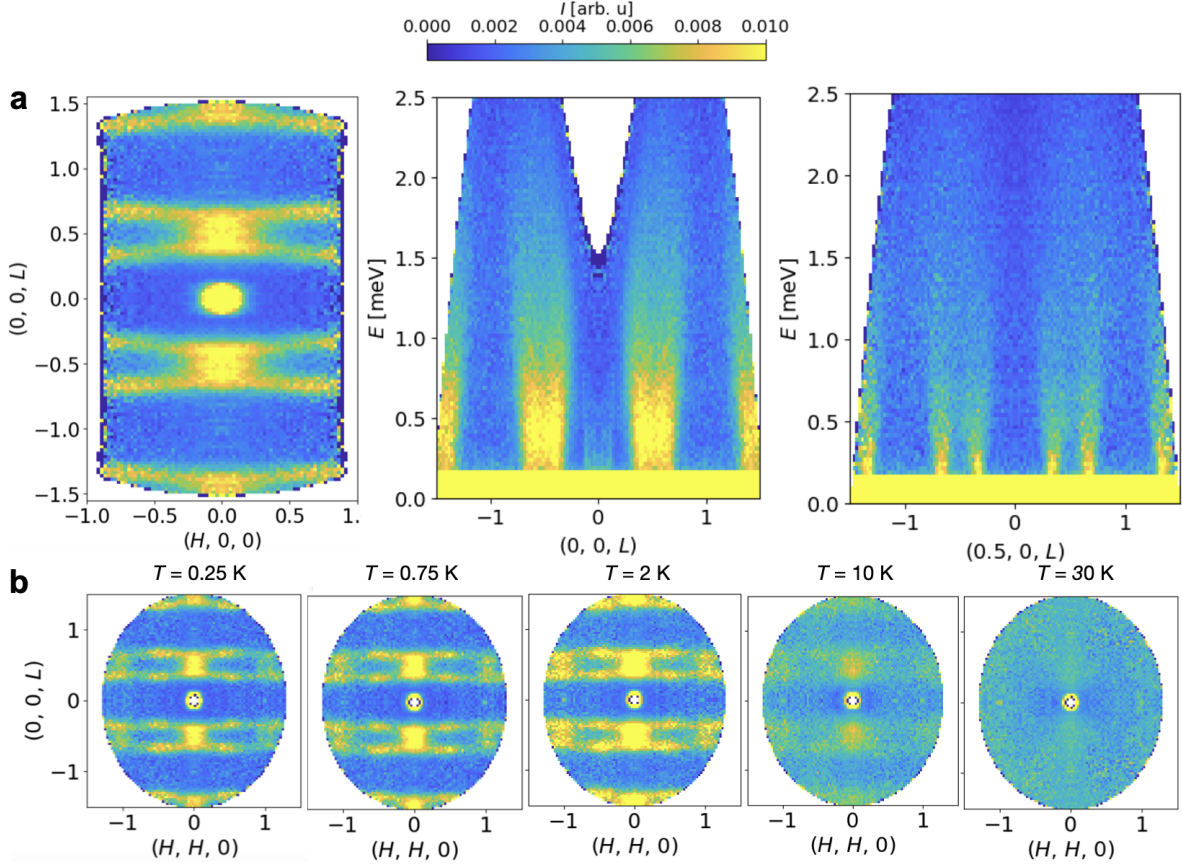


FIG. 3. **Dynamic properties of YbAgGe.** **a** Magnetic excitation spectrum at $T = 0.25$ K and $\mu_0 H = 0$ T in the $(H, 0, L)$ plane at an energy transfer $E = 0.3$ meV, along $(0, 0, L)$ and $(1/2, 0, L)$. The data were measured on CNCS using an incident energy $E_i = 3.32$ meV and plotted with an energy integration $\Delta E = [0.2, 0.4]$ meV and reciprocal space integration $\Delta Q = [-0.1, 0.1]$ rlu in the first subpanel, and $\Delta Q = \pm 0.1$ rlu perpendicular to the $(0, 0, L)$ and $(1/2, 0, L)$ directions. **b** Reciprocal space maps of the (H, H, L) plane at an energy transfer $E = 0.3$ meV at $T = 0.25, 0.75, 2, 10$ and 30 K. The data were measured with $E_i = 3.32$ meV using an energy integration range $\Delta E = [0.2, 0.4]$ meV and $\Delta Q = [-0.1, 0.1]$ rlu perpendicular to the (H, H, L) plane.

the spectrum also features an anisotropy in the Kagome plane. The excitations are column-like with decreasing intensity as function of energy transfer. No clear excitation gap was observed, so we fitted the dynamic susceptibility with a quasielastic Lorentzian following previous inelastic neutron scattering experiments²⁷ (see SI Note 6). The results show that the excitations are overdamped with a wavevector dependent relaxation rate that is smallest at $q = (0, 0, 1/2)$ (0.23(7) meV), almost double (0.41(6) meV) at $q = (0, 0, 1/3)$ and 0.54(7) meV on average.

Remarkably, the magnetic excitation spectrum is not affected by moderate temperature changes. In Fig. 3b we display reciprocal space maps of the (H, H, L) plane for $E = 0.3$ meV measured at $T = 0.25, 0.75, 2, 10$ and 30 K. The results imply that magnetic fluctuations are unaffected by magnetic long-range order at $T_N = 0.68$ K. Notably, they are gradually weakened and suppressed only above $T^* \approx 20$ K (see SI Note 6 for details), match-

ing the unusual temperature dependence of the electronic resistivity (see Fig. 1b). The INS spectra also reveal a nontrivial behaviour under magnetic field. Our results measured at CAMEA with $T = 50$ mK and $H \parallel [1, -1, 0]$ show that the magnetic fluctuations are only modified above $\mu_0 H \geq 7$ T where magnetic long-range order with $q_z \approx 1/3$ is suppressed (see SI Note 7 and Ref.²³). In fact, at $\mu_0 H = 11$ T we find that the excitations develop a dispersion along $(0, 0, L)$ that is quasielastic at $(0, 0, 1/3)$ and $(0, 0, 2/3)$ and reaches a maximum at $(0, 0, 1)$ with an energy transfer $E \sim 3.5$ meV (see Fig. 4). The full-width at half-maximum of the magnetic excitation on top of the dispersion is $\Delta E = 1.03(8)$ meV, providing evidence for a finite excitation life time.

We used a variety of local-moment Hamiltonians that retain $q_z \approx 1/3$ to reproduce the magnetic excitation spectrum along $(0, 0, L)$. Notably, we considered one-dimensional Heisenberg chains with an axial CEF anisotropy, anisotropic xxz -exchange interactions

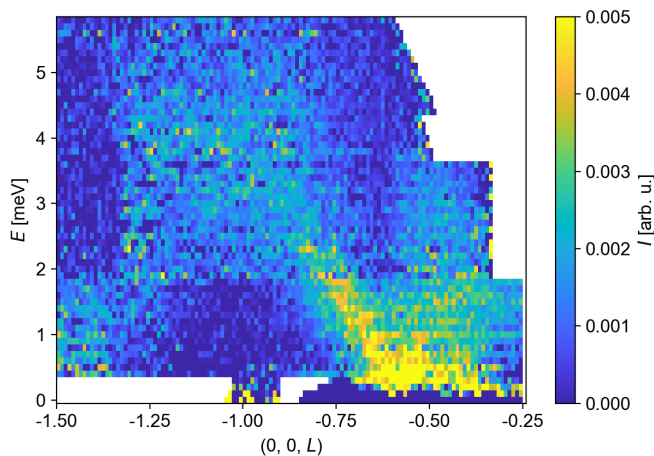


FIG. 4. **Dynamic properties in magnetic field.** Magnetic excitation spectrum at $T = 0.05$ K and $\mu_0 H = 11$ T along $(0, 0, L)$. The background subtracted data were measured at CAMEA with a reciprocal space integration $\Delta Q = [-0.25, 0.25]$ rlu along the $(H, H, 0)$ direction.

allowed by the crystal structure, and tested the effect of a magnetic field along $H \parallel [1, -1, 0]$ (see SI Note 8 for details). As expected, we find that even a small anisotropy induces a finite gap in the excitation spectrum, contrasting the experimental observations at zero field and under magnetic field. This further supports that the microscopic nature of the magnetic properties in YbAgGe go beyond the localized-moment picture.

Discussion

YbAgGe is an intricate system showing elements of magnetic frustration, local moment and itinerant electrons physics. Our diffuse neutron scattering results shown in Fig. 2b highlight that magnetic frustration stemming from the distorted Kagome plane and from orthogonal chain interactions play an important role in the material. Localised exchange Hamiltonians are the standard approach for insulators and are also appropriate for metals possessing only a small density of states at the Fermi surface²⁸. However, this approach is inappropriate for metals like YbAgGe, because the strong interactions between local magnetic moments and itinerant electrons trigger preeminent hybrid excitations fainted by substantial damping effects^{29–34}. One such example with qualitative similarities to YbAgGe is the frustrated Kagome lattice TbMn_6Sn_6 ^{32–34}. The material features sharp acoustic magnons and overdamped flat-band excitations that induce in-plane structure factor patterns broadly resembling the diffuse scattering we observe in YbAgGe above T_N (see Fig. 2). The excitations in TbMn_6Sn_6 originate from flat-bands and chiral fluctuations localised on hexagonal plaquettes. However, since the ordered magnetic structure of YbAgGe is amplitude modulated and the moment directions are pinned by the CEF anisotropy, these short-range correlations are possibly governed by different fluctuations.

Most magnets with prominent itinerancy require magnetic Hamiltonians which account for the electronic-band structure^{35–37}. However, the small energy differences between different electronic configurations in Kondo metals still cause severe difficulties in theoretically predicting the electronic properties with sufficient accuracy, which complicates a mapping onto reliable effective Hamiltonians. Progress has been made in model cases of non-magnetic magnetic Kondo metals crystallizing in simple cubic lattice structures such as CeX_3 ($X = \text{Pd}, \text{In}$)^{35–37}. Here microscopic theoretical predictions have become possible, but their extension to complex structures such as non-centrosymmetric YbAgGe is not yet available. This step is required to quantitatively assess the effect of magnetic frustration in this material class. In fact, an intermediate route succeeding with this endeavor may include theoretical investigations of itinerant frustrations hosting Kondo inactive $4f$ -ions. Examples include other materials in the $R\text{AgGe}$ family, also revealing unusual frustrated quantum phases without the additional complexities imposed by the Kondo exchange interaction^{22,38,39}. Such studies are important to deepen our understanding of how frustration is established in metallic hosts.

On a qualitative level our various experimental observations can be grouped into four different temperature regions. Above $T > T^* \approx 20$ K YbAgGe behaves like a paramagnetic intermetallic material. As the temperature is decreased below T^* a significant coupling between the itinerant electrons and the local magnetic moments is evidenced by the coincident change in the resistivity versus temperature behaviour and the emergence of spin-spin correlations in the INS data (see Figs. 1c and 3). The similarity to other Kondo metals³⁵ suggests that the coupling in YbAgGe arises via Kondo screening leading to hybridized Yb-bands with coherent inter-band excitations. If so, the field dependence of the magnetic excitations further suggests that the hybridized Yb-bands are located in the eminent vicinity of the Fermi surface, because they are affected at moderate fields already. Confirmation of this hypothesis requires detailed knowledge of the Fermi surface topology, which can be gained using angle-resolved photoemission spectroscopy, scanning tunneling microscope spectroscopy or De Haas-Van Alphen techniques. Unfortunately, technical challenges have restricted success of these methods in YbAgGe so far.

Below $T_{SR} \approx 2$ K the magnetic properties change²⁴. For $0.68 \text{ K} < T < T_{SR}$ we find evidence for magnetic short-range correlations centered around $q = (0, 0, 1/3)$, and long-range along the c -direction (see Fig. 2). The liquid-like state reveals similarities to a smectic phase with one long-range correlated axis only. While future theoretical efforts are required to elucidate the microscopic nature of this putative spin liquid-like phase, we find that it reveals growing correlations along the c -direction when the temperature is lowered while correlations in the ab -plane remain short-ranged (see SI Note 4). Using the localized Heisenberg picture our analysis

suggests AFM J_1 and J_2 couplings in the Kagome plane, and equal sized J_{c1} and J_{c2} interplane couplings to realize $q = (0, 0, 1/3)$.

Below $T_N = 0.68$ K magnetic long-range order is established along $q = (1/3, 0, 1/3)$, in which in-plane ordering requires AFM J_{c1} and J_{c2} couplings and finite further neighbour terms in a localized picture (see SI Note 3). The diffraction results²³ report a significantly-reduced magnetic moment of $\mu_{ord} \approx 1.6\mu_B$ with respect to the expected localized moment of $\mu_{CEF} = 3.98\mu_B$ obtained from the CEF ground state wavefunction. These observations ascertain that a localized picture provides only a limited view, so that the itineracy plays an important role. This may be reflected also in the stability of $q_z \approx 1/3$, which can be interpreted as robust Fermi surface nesting along the c -axis, resisting changes induced by an applied magnetic field. Along these lines the field modifications in q_x and q_y indicate almost degenerate nesting conditions in the hexagonal plane that can be tuned with magnetic field. The hypothesis is also supported by our inelastic neutron scattering results revealing an enhanced low-energy spectral weight along $(H, K, 1/3)$. The enhanced spectral weight around $(0, 0, 1/2)$ may further originate from competing nested Fermi surface sheets at larger energy transfers (see SI Note 6 for details).

Summary

The intricate interaction between the conduction electrons and localized moments in magnetic Kondo metals allow for the exploration of novel frustrated phases, whose interpretation remains challenging. In YbAgGe we observe enhanced dynamic fluctuations of $4f$ Yb-moments below $T^* \approx 20$ K. Below $T_{SR} \approx 2$ K the interaction between the itinerant electrons and local magnetic moments are modified, giving rise to a liquid-like state, which can be partially modeled via a localised Heisenberg Hamiltonian with AFM intraplane couplings. Magnetic long-range order is established below $T_N = 0.68$ K, suggesting AFM nearest-neighbour interplane couplings and finite further-neighbour terms. Altogether these experimental findings allude the following hierarchy of rather close energy scales $E_{CEF}^{splitting} > E_{KLH}^{exchange} \geq E_{frustrated}^{interactions}$. The case of YbAgGe testifies that effective model Hamiltonians that encode the electronic Fermi surface are required to accurately predict the microscopic properties of frustrated Kondo metals.

Methods

Crystal synthesis and macroscopic measurements. YbAgGe single crystals were grown from Ag- and Ge-rich high-temperature solutions and characterized as described in Ref.²⁶. Sizable single crystals appropriate for inelastic neutron scattering were obtained through optimization of the synthesis process such as described in Ref.²³ and⁴⁰ (see SI Note 1). Electric resistivity was measured down to $T = 1.8$ K using a Quantum Design PPMS-14 instrument. We used a standard AC four probe resistance technique ($f = 16$ Hz, $I = 1$ -0.3 mA), where Pt leads were attached to a surface-polished YbAgGe single crystal using Epotek H2OE silver epoxy

so that the current was flowing either along the crystallographic c -direction or within the ab -plane. The magnetization experiments in pulsed magnetic fields up to $\mu_0 H = 50$ T were performed at the Dresden High Magnetic Field Laboratory. We used a compensated pickup-coil system in a pulse-field magnetometer with a home-built ^4He cryostat and a pulsed magnet with an inner bore of 20 mm that was powered by a 1.44 MJ capacitor bank⁴¹.

Crystal electric field measurements. The crystal electric-field scheme of YbAgGe was probed at $T = 3$ K on a powdered sample enclosed in an Al can. The data were measured on the time-of-flight spectrometer MARI at ISIS Neutron and Muon Source, UK, using an incident neutron beam of $E_i = 49.75$ meV with an elastic energy resolution of 3.98(2) meV full-width at half-maximum (FWHM). The spectrum with a wavevector transfer $|q| < 4 \text{ \AA}^{-1}$ was fitted to two resolution-limited Gaussian peaks revealing CEF transitions centered at $E = 12.0(4)$ meV. An additional peak emerges at $E = 23(1)$ meV for $6 < |q| < 10 \text{ \AA}^{-1}$. The energy spectrum was analyzed using the PyCrystalField software package²¹. Further information can be found in SI Note 2.

Static and dynamic magnetism at zero magnetic field. The static and dynamic properties at $\mu_0 H = 0$ T and $T = 0.25$ - 30 K were studied on the Cold Neutron Chopper Spectrometer (CNCS) at the Spallation Neutron Source (SNS), Oak Ridge National Laboratory, USA. A $m \sim 2.5$ g crystal oriented with (H, H, L) in the horizontal scattering plane was measured for 20 or 40 s per point over an angular range of 180 or 360° with a step size of 0.5°. We used incident energies $E_i = 12, 3.32$ and 1.55 meV with chopper frequencies of 180 Hz on both double disk choppers, resulting in elastic energy resolutions $\Delta E = 1.2, 0.175$ and 0.04 meV FWHM. The data was reduced with the Mantid software package⁴² and folded using the symmetry operations of $P\bar{6}2m$.

The magnetic field dependence of the dynamic properties were measured on the cold neutron multiplexing spectrometer CAMEA at the Paul Scherrer Institut, Switzerland⁴³. The sample with $m \sim 4$ g consisted of two single crystals that were coaligned within 1° in the horizontal (H, H, L) plane. We used a vertical 11 T magnet with dilution insert enabling measurements down to $T = 50$ mK. For $\mu_0 H = 0, 2$ and 5.5 T we used an incident energy $E_i = 5$ meV, providing an elastic line resolution of $\Delta E = 0.19$ meV FWHM (see also SI Note 6). At $\mu_0 H = 11$ T we used combination of different incident energies $E_i = 3.6, 5, 6.8, 7.8, 8.7$ and 9.6 meV with elastic line resolution of $\Delta E = 0.11$ meV FWHM. The 60° wide detector was set at angles to cover a reciprocal space range of $\sim 0.5 < |q| < \sim 2.3 \text{ \AA}^{-1}$ in the horizontal scattering plane optimized to follow the magnetic signal. We used a sample rotation step size of 0.5° to cover an angular range of 240° for detector settings $|q| < \sim 1.5 \text{ \AA}^{-1}$, and 120° for $\sim 0.8 < |q| < \sim 2.3 \text{ \AA}^{-1}$. About 25 h of statistics was collected at $\mu_0 H = 0, 2$ and 5.5 T, and 71 h for $\mu_0 H = 11$ T. The data was reduced with the MJOLNIR software package⁴⁴. The background subtraction was per-

formed via a powder average over the (q, E) range where no signal was present, similar to Refs.^{45,46}.

ACKNOWLEDGEMENTS

We thank D. McMorro and Ch. Rüegg for sharing their earlier results on YbAgGe. We acknowledge fruitful discussions with Ch. Rüegg, P. Orth, N. Gauthier, J. Lass, P. Baral, H. D. Rosales, F. A. G. Albarracín, C. Batista and M. Janoschek. This work received financial support from the Swiss National Science Foundation (Grants No. 200020_182536, 200021_200653). This research used resources at the Spallation Neutron Source (proposal number IPTS 3207), Department of Energy (DOE) Office of Science User Facilities operated by Oak Ridge National Laboratory (ORNL). We acknowledge the Paul Scherrer Institut for the allocated beamtime on CAMEA (Proposal No. 20212894). We acknowledge the support of the HLD at HZDR, a member of the European Magnetic Field Laboratory (EMFL). Work done at Ames National Laboratory was supported by the U.S. Department of Energy, Office of Basic Energy Science, Division of Materials Sciences and Engineering. Ames National Laboratory is operated for the U.S. Department of Energy by Iowa State University under Contract No. DE-AC02-07CH11358.

AUTHOR CONTRIBUTIONS

The project was conceived and initiated by D.G.M., O.Z. P.C.C., S.L.B., B.F. and Ch.R. The samples were

synthesised and characterized by P.C.C. and S.L.B., D.G.M., C.B.L., B.U., X.B., R.B., D.M.P, Y.S., J.T., S.L.B., R.M., P.C.C. and O.Z. prepared and performed the experiments. D.G.M., B.U., S.L.B., R.M., P.C.C. and O.Z. analyzed and interpreted the experimental data. The paper was written by D.G.M., B.U., S.L.B., R.M., P.C.C. and O.Z. with the input from all co-authors.

ADDITIONAL INFORMATION

Correspondence and requests for materials should be addressed to D.G.M. or O.Z.

COMPETING FINANCIAL INTERESTS

The authors declare no competing interests.

DATA AVAILABILITY

The data is available from the authors upon reasonable request.

CODE AVAILABILITY

The code used to analyze the data presented in this study is available from the authors upon reasonable request.

* daniel.mazzone@psi.ch

† oksana.zaharko@psi.ch

¹ Fert, A., Reyren, N. & Cros, V. Magnetic skyrmions: advances in physics and potential applications. *Nature Reviews Materials* **2**, 17031 (2017). URL <https://doi.org/10.1038/natrevmats.2017.31>.

² Mydosh, J. *Spin Glasses: An Experimental Introduction* (Taylor & Francis, 1993). URL <https://books.google.ch/books?id=NcIYzgEACAAJ>.

³ Balents, L. Spin liquids in frustrated magnets. *Nature* **464**, 199–208 (2010). URL <https://doi.org/10.1038/nature08917>.

⁴ Starykh, O. A. Unusual ordered phases of highly frustrated magnets: a review. *Reports on Progress in Physics* **78**, 052502 (2015). URL <https://dx.doi.org/10.1088/0034-4885/78/5/052502>.

⁵ Broholm, C. et al. Quantum spin liquids. *Science* **367**, eaay0668 (2020).

⁶ Hayami, S. & Motome, Y. Topological spin crystals by itinerant frustration. *Journal of Physics: Condensed Matter* **33**, 443001 (2021). URL <https://dx.doi.org/10.1088/1361-648X/ac1a30>.

⁷ Al-Hassanieh, K. A., Yang, Y.-F., Martin, I. & Batista, C. D. Effective low-energy model for f -electron delocalization. *Phys. Rev. Lett.* **105**, 086402 (2010). URL <https://link.aps.org/doi/10.1103/PhysRevLett.105.086402>.

⁸ Stewart, G. R. Non-Fermi-liquid behavior in d - and f -electron metals. *Rev. Mod. Phys.* **73**, 797–855 (2001). URL <https://link.aps.org/doi/10.1103/RevModPhys.73.797>.

⁹ Ruderman, M. A. & Kittel, C. Indirect exchange coupling of nuclear magnetic moments by conduction electrons. *Phys. Rev.* **96**, 99–102 (1954). URL <https://link.aps.org/doi/10.1103/PhysRev.96.99>.

¹⁰ Kasuya, T. A Theory of Metallic Ferro- and Antiferromagnetism on Zener's Model. *Progress of Theoretical Physics* **16**, 45–57 (1956). URL <https://doi.org/10.1143/PTP.16.45>. <https://academic.oup.com/ptp/article-pdf/16/1/45/5266722/16-1-45.pdf>.

¹¹ Yosida, K. Magnetic properties of Cu-Mn alloys. *Phys. Rev.* **106**, 893–898 (1957). URL <https://link.aps.org/doi/10.1103/PhysRev.106.893>.

¹² Lacroix, C. Frustrated metallic systems: A review of some peculiar behavior. *Journal of the Physical Society of Japan* **79**, 011008

- (2010). URL <https://doi.org/10.1143/JPSJ.79.011008>.
- ¹³ Stockert, O. et al. Magnetic frustration in a metallic *fcc* lattice. *Phys. Rev. Res.* **2**, 013183 (2020). URL <https://link.aps.org/doi/10.1103/PhysRevResearch.2.013183>.
 - ¹⁴ Kurumaji, T. et al. Skyrmion lattice with a giant topological Hall effect in a frustrated triangular-lattice magnet. *Science* **365**, 914–918 (2019). URL <https://www.science.org/doi/abs/10.1126/science.aau0968>. <https://www.science.org/doi/pdf/10.1126/science.aau0968>.
 - ¹⁵ Gao, S. et al. Spiral spin-liquid and the emergence of a vortex-like state in MnSc_2S_4 . *Nature Physics* **13**, 157–161 (2017). URL <https://doi.org/10.1038/nphys3914>.
 - ¹⁶ Kondo, J. Resistance minimum in dilute magnetic alloys. *Progress of Theoretical Physics* **32**, 37–49 (1964). URL <https://doi.org/10.1143/PTP.32.37>. <https://academic.oup.com/ptp/article-pdf/32/1/37/5193092/32-1-37.pdf>.
 - ¹⁷ Hewson, A. C. *The Kondo problem to heavy fermions*. 2 (Cambridge university press, 1997).
 - ¹⁸ Gibson, B., Pöttgen, R., Kremer, R. K., Simon, A. & Ziebeck, K. R. A. Ternary germanides LnAgGe ($\text{Ln} = \text{Y}, \text{Sm}, \text{Gd-Lu}$) with ordered Fe_2P -type structure. *J. Alloys Compounds* **239**, 34 (1996).
 - ¹⁹ Matsumura, T. et al. Spin fluctuation and crystal field excitation of heavy-fermion compound YbAgGe studied by inelastic neutron scattering. *Journal of the Physical Society of Japan* **73**, 2967–2970 (2004). URL <https://doi.org/10.1143/JPSJ.73.2967>. <https://doi.org/10.1143/JPSJ.73.2967>.
 - ²⁰ Bonville, P. et al. Magnetic structures and crystal field in the heavy electron materials YbAgGe and YbPtIn . *The European Physical Journal B* **55**, 77–84 (2007). URL <https://doi.org/10.1140/epjb/e2007-00042-6>.
 - ²¹ Scheie, A. *PyCrystalField*: software for calculation, analysis and fitting of crystal electric field Hamiltonians. *Journal of Applied Crystallography* **54**, 356–362 (2021). URL <https://doi.org/10.1107/S160057672001554X>.
 - ²² Larsen, C. B. et al. Magnetic ground state and perturbations of the distorted kagome Ising metal TmAgGe . *Phys. Rev. B* **107**, 224419 (2023). URL <https://link.aps.org/doi/10.1103/PhysRevB.107.224419>.
 - ²³ Larsen, C. B. et al. Ubiquity of amplitude-modulated magnetic ordering in the H-T phase diagram of the frustrated non-Fermi-liquid YbAgGe . *Phys. Rev. B* **104**, 054424 (2021). URL <https://link.aps.org/doi/10.1103/PhysRevB.104.054424>.
 - ²⁴ Bud'ko, S. L., Morosan, E. & Canfield, P. C. Magnetic field induced non-Fermi-liquid behavior in YbAgGe single crystals. *Phys. Rev. B* **69**, 014415 (2004). URL <https://link.aps.org/doi/10.1103/PhysRevB.69.014415>.
 - ²⁵ Paddison, J. A. M. Ultrafast calculation of diffuse scattering from atomistic models. *Acta. Cryst. A* **75**, 14–24 (2019). URL <https://doi.org/10.1107/S2053273318015632>.
 - ²⁶ Morosan, E., Bud'ko, S., Canfield, P., Torikachvili, M. & Lacerda, A. Thermodynamic and transport properties of RAgGe ($\text{R}=\text{Tb-Lu}$) single crystals. *Journal of Magnetism and Magnetic Materials* **277**, 298–321 (2004). URL <https://www.sciencedirect.com/science/article/pii/S0304885303009260>.
 - ²⁷ Fåk, B. et al. An inelastic neutron scattering study of single-crystal heavy-fermion YbAgGe . *Journal of Physics: Condensed Matter* **17**, 301 (2004). URL <https://dx.doi.org/10.1088/0953-8984/17/2/006>.
 - ²⁸ Boraley, X. et al. Microscopic origin of reduced magnetic order in a frustrated metal. *Phys. Rev. Lett.* **135**, 046702 (2025). URL <https://link.aps.org/doi/10.1103/38ds-xjl3>.
 - ²⁹ Halloran, T. et al. Connection between *f*-electron correlations and magnetic excitations in UTe_2 . *npj Quantum Materials* **10**, 2 (2025). URL <https://doi.org/10.1038/s41535-024-00720-9>.
 - ³⁰ Chen, X. et al. Unconventional Hund metal in a weak itinerant ferromagnet. *Nature Communications* **11**, 3076 (2020). URL <https://doi.org/10.1038/s41467-020-16868-4>.
 - ³¹ Rossat-Mignod, J. et al. Inelastic neutron scattering study of cerium heavy fermion compounds. *Journal of Magnetism and Magnetic Materials* **76–77**, 376–384 (1988).
 - ³² Riberolles, S. X. M. et al. Chiral and flat-band magnetic quasiparticles in ferromagnetic and metallic kagome layers. *Nature Communications* **15**, 1592 (2024). URL <https://doi.org/10.1038/s41467-024-45841-8>.
 - ³³ Riberolles, S. X. M. et al. Orbital character of the spin-reorientation transition in TbMn_6Ss_6 . *Nature Communications* **14**, 2658 (2023).
 - ³⁴ Riberolles, S. X. M. et al. Low-temperature competing magnetic energy scales in the topological ferrimagnet TbMn_6Ss_6 . *Phys. Rev. X* **12**, 021043 (2022). URL <https://link.aps.org/doi/10.1103/PhysRevX.12.021043>.
 - ³⁵ Goremychkin, E. A. et al. Coherent band excitations in CePd_3 : A comparison of neutron scattering and *ab initio* theory. *Science* **359**, 186–191 (2018). URL <https://www.science.org/doi/abs/10.1126/science.aan0593>. <https://www.science.org/doi/pdf/10.1126/science.aan0593>.
 - ³⁶ Simeth, W. et al. A microscopic Kondo lattice model for the heavy fermion antiferromagnet CeIn_3 . *Nature Communications* **14**, 8239 (2023). URL <https://doi.org/10.1038/s41467-023-43947-z>.
 - ³⁷ Ghioldi, E. A. et al. Derivation of low-energy Hamiltonians for heavy-fermion materials. *Phys. Rev. B* **110**, 195123 (2024). URL <https://link.aps.org/doi/10.1103/PhysRevB.110.195123>.
 - ³⁸ Zhao, K. et al. Realization of the kagome spin ice state in a frustrated intermetallic compound. *Science* **367**, 1218–1223 (2020). URL <https://www.science.org/doi/abs/10.1126/science.aaw1666>. <https://www.science.org/doi/pdf/10.1126/science.aaw1666>.
 - ³⁹ Bhandari, H. et al. Tunable topological transitions in the frustrated magnet HoAgGe (2024). URL <https://arxiv.org/abs/2410.11636>. 2410.11636.
 - ⁴⁰ Canfield, P. C. New materials physics. *Reports on Progress in Physics* **83**, 016501 (2019). URL <https://dx.doi.org/10.1088/1361-6633/ab514b>.
 - ⁴¹ Skourski, Y., Kuz'min, M. D., Skokov, K. P., Andreev, A. V. & Wosnitza, J. High-field magnetization of $\text{Ho}_2\text{Fe}_{17}$. *Phys. Rev. B* **83**, 214420 (2011). URL <https://link.aps.org/doi/10.1103/PhysRevB.83.214420>.
 - ⁴² Arnold, O. et al. Mantid-data analysis and visualization package for neutron scattering and μSR experiments. *Nuclear Instruments and Methods in Physics Research. Section A: Accelerators, Detectors and Electronic Instrumentation* **764**, 156–166 (2014). URL <https://www.sciencedirect.com/science/article/pii/S0168900214008729>.
 - ⁴³ Lass, J. et al. Commissioning of the novel Continuous Angle Multi-Energy Analysis spectrometer at the Paul Scher-

- rer Institut. *Rev. Sci. Instrum.* **94**, 023302 (2023). URL <https://doi.org/10.1063/5.0128226>.
- ⁴⁴ Lass, J., Jacobsen, H., Mazzone, D. G. & Lefmann, K. Mjolnir: A software package for multiplexing neutron spectrometers. *SoftwareX* **12**, 100600 (2020). URL <https://www.sciencedirect.com/science/article/pii/S2352711020303137>.
- ⁴⁵ Sala, G. et al. Field-tuned quantum renormalization of spin dynamics in the honeycomb lattice Heisenberg antiferromagnet YbCl₃. *Communications Physics* **6**, 234 (2023). URL <https://doi.org/10.1038/s42005-023-01333-7>.
- ⁴⁶ Facheris, L. et al. Spin density wave versus fractional magnetization plateau in a triangular antiferromagnet. *Phys. Rev. Lett.* **129**, 087201 (2022). URL <https://link.aps.org/doi/10.1103/PhysRevLett.129.087201>.
- ⁴⁷ Toth, S. et al. Linear spin wave theory for single-Q incommensurate magnetic structures. *J. Phys.: Condens. Matter* **27**, 166002 (2015). URL <https://doi.org/10.1088/0953-8984/27/16/166002>.
- ⁴⁸ Schmiedeshoff, G. M. et al. Multiple regions of quantum criticality in YbAgGe. *Phys. Rev. B* **83**, 180408 (2011). URL <https://link.aps.org/doi/10.1103/PhysRevB.83.180408>.

Supplemental Material for: Microscopic Origin of Reduced Magnetic Order in a Frustrated Metal

D. G. Mazzone,^{1,*} C. B. Larsen,¹ B. Ueland,^{2,3} X. Boraley,¹ D. M. Pajerowski,⁴ Y. Skourski,⁵ J. Taylor,⁶ B. Fåk,⁷ S. L. Bud'ko,^{2,3} R. McQueeney,^{2,3} P. C. Canfield,^{2,3} and O. Zaharko^{1,†}

¹*PSI Center for Neutron and Muon Sciences, 5232 Villigen PSI, Switzerland*

²*Department of Physics and Astronomy, Iowa State University, Ames, Iowa 50011, USA*

³*Ames National Laboratory, Iowa State University, Ames, Iowa 50011, USA*

⁴*Neutron Scattering Division, Oak Ridge National Laboratory, Oak Ridge, Tennessee 37831, USA*

⁵*Dresden High Magnetic Field Laboratory (HLD-EMFL),
Helmholtz-Zentrum Dresden-Rossendorf, 01328 Dresden, Germany*

⁶*ISIS Facility, STFC Rutherford Appleton Laboratory,
Harwell Science and Innovation Campus, Oxfordshire OX11 0QX, United Kingdom*

⁷*Institut Laue-Langevin, 71 Avenue des Martyrs, CS20156, 38042 Grenoble Cédex 9, France*

(Dated: September 3, 2025)

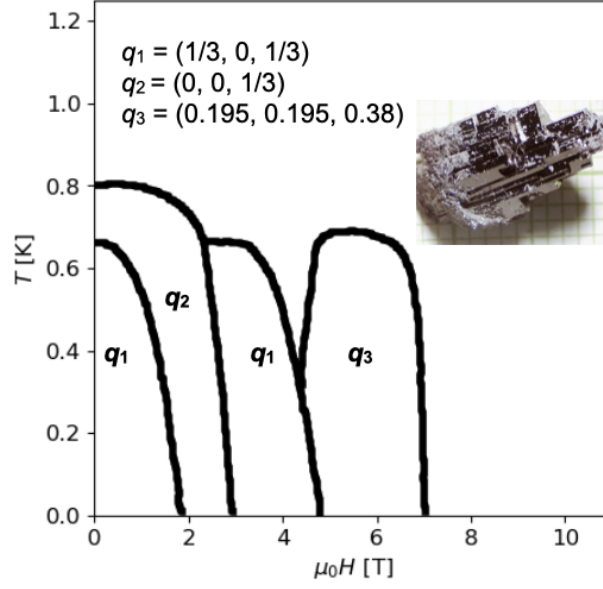
SUPPLEMENTARY NOTE 1: SINGLE CRYSTAL GROWTH AND MAGNETIC PHASE DIAGRAM

YbAgGe single crystals were grown from a Ag- and Ge-rich high-temperature ternary solution⁴⁰ and characterized based on the procedure described in Ref.²⁶. In order to grow a significant number of large single crystals of YbAgGe, the growth was optimized in several ways. Roughly 10 g of high purity Yb, Ag, and Ge were placed in a 5 ml Al₂O₃ crucible in a molar ratio of Yb0:14Ag0:645Ge0:215. The Yb with 99.99+% purity was obtained from the Ames Laboratory Materials Preparation Center. A second 5 ml Al₂O₃ crucible, filled with silica wool, was placed on top of the growth crucible to act as a filter and catch for excess liquid²⁶. The growth and catch crucibles were sealed into an evacuated amorphous silica tube and placed in a resistively heated box furnace. In order to partially control nucleation, the growth ampoules were placed close to the inner edges of the furnace door. We found that larger crystals often grew on the side of the crucible facing this colder spot in the furnace. The furnace was heated to 1100 °C over 4 hours, and heated further to 1190 °C over an additional hour. The furnace was then cooled to 1090 °C over 5 hours and then slow cooled to 840 °C over 200 hours. The growth ampoules were removed from the furnace at 840 °C and placed in a centrifuge⁴⁰ for separation of the excess liquid from the YbAgGe single crystals. Depending on nucleation, single crystals as large as 1 - 2 grams could be obtained (see inset of Fig. S1).

Antiferromagnetic (AFM) long-range order in YbAgGe is established below $T_N = 0.68$ K with a propagation vector $q = (1/3, 0, 1/3)$ ²³. A magnetic field applied in the Kagome plane triggers a series of metamagnetic transitions to other magnetic states with different periodicity as shown in Fig. 1. Above $\mu_0 H \approx 7$ T ($H \parallel [1, -1, 0]$) these modulations vanish, so that eventually only an induced FM component remains. We mention that previous macroscopic studies revealed additional correlated signatures in the HT -phase diagram of YbAgGe⁴⁸.

SUPPLEMENTARY NOTE 2: CRYSTAL-ELECTRIC FIELD REFINEMENT

The energy spectrum of a polycrystalline YbAgGe sample measured on the MARI spectrometer at ISIS with $E_i = 49.75$ meV and $T = 3$ K revealed nondispersing excitations at $E = 12.0(4)$, $23(1)$ and $36(1)$ meV. The first feature reveals intensity prevailing below the wavevector transfers $|q| < 4 \text{ \AA}^{-1}$, which we attributed to a crystal-electric field (CEF) transition. Fits of this transition against the CEF Hamiltonian $H_{CEF} = \sum_{n,m} B_n^m O_n^m$, with O_n^m being Stevens operators and B_n^m CEF parameters by PyCrystalField python package²¹ using the z-direction as the local quantization axis reveal $B_2^0 \approx 0.124$ meV, $B_2^2 \approx -1.27$ meV and negligible higher order CEF parameters. The



Supplemental Figure 1. Schematic HT -phase diagram for $H||[1, -1, 0]$. Schematic magnetic phase diagram of magnetic long-range order in YbAgGe for $H||[1, -1, 0]$ with corresponding magnetic wavevectors q_{1-3} . The diagram has been reproduced from Ref.²³. Inset: Picture of a YbAgGe single crystal.

TABLE S1. Eigenvectors and eigenvalues of the CEF scheme of the Yb^{3+} ion in YbAgGe.

E (meV)	$ \pm \frac{7}{2}\rangle$	$ \pm \frac{5}{2}\rangle$	$ \pm \frac{3}{2}\rangle$	$ \pm \frac{1}{2}\rangle$	$ \frac{1}{2}\rangle$	$ \frac{3}{2}\rangle$	$ \frac{5}{2}\rangle$	$ \frac{7}{2}\rangle$
0.000	-0.1927	0.0	-0.5777	0.0	-0.6921	0.0	-0.3875	0.0
0.000	0.0	-0.3875	0.0	-0.6921	0.0	-0.5777	0.0	-0.1927
11.997	-0.5474	0.0	-0.5126	0.0	0.2337	0.0	0.6189	0.0
11.997	0.0	-0.6189	0.0	-0.2337	0.0	0.5126	0.0	0.5474
19.608	0.0	0.5358	0.0	-0.2763	0.0	-0.2779	0.0	0.7479
19.608	-0.7479	0.0	0.2779	0.0	0.2763	0.0	-0.5358	0.0
27.764	0.3222	0.0	-0.5713	0.0	0.6245	0.0	-0.424	0.0
27.764	0.0	0.424	0.0	-0.6245	0.0	0.5713	0.0	-0.3222

resulting set of eigenvectors and eigenvalues are shown in Tabl. S1, establishing a ground state doublet $|\Psi^\pm\rangle = -0.1927|\pm 7/2\rangle - 0.3875|\pm 5/2\rangle - 0.5777|\pm 3/2\rangle - 0.6921|\pm 1/2\rangle$ with a localized moment of $\mu_{CEF} = 3.98\mu_B$ and significant axial anisotropy, g -tensor = (7.954, 0.0278, 0.0357). Attempts to include the second and third peaks with intensity dominating at $6 < |q| < 10 \text{ \AA}^{-1}$ destabilized the refinement and worsen the fit of the $E = 12.0(4) \text{ meV}$ transition. Along with the $|q|$ dependence this suggests a phononic origin of these excitations.

In a localised moment picture the ground state doublet $|\Psi^\pm\rangle$ is split by magnetic long-range order. Thus, the dipole allowed transitions between the ground state wavefunctions give an estimation of the neutron cross-section expected in the ordered state. For YbAgGe we find $\langle \Psi^+ | J_x | \Psi^- \rangle = 3.48$, $\langle \Psi^+ | J_y | \Psi^- \rangle = 0.0121$ and $\langle \Psi^+ | J_z | \Psi^- \rangle = 0$. The strongest component indicates the preferred ordered moment direction which is the local x-axis of the three magnetic Yb sites, *i.e.* (1, 0, 0) for Yb1, (0, 1, 0) for Yb2 and (1, 1, 0) for Yb3 (see also Ref.²³). The other components give a cross-section estimation for the magnetic fluctuations perpendicular to the ordered moment. Their small value indicate very weak spin-wave excitations that are expected to be hardly observable in an inelastic neutron scattering experiment.

SUPPLEMENTARY NOTE 3: INSIGHT INTO EXCHANGE COUPLINGS

Despite various contributing ingredients in frustrated metals, it is often possible to determine the main couplings through a localised Heisenberg exchange Hamiltonian. For YbAgGe we used the effective Hamiltonian

$$H = \sum_{ij} J_{ij} \mathbf{S}_i \cdot \mathbf{S}_j + \sum_{ij} J_{cij} \mathbf{S}_i \cdot \mathbf{S}_j + A \sum_i \mathbf{S}_i^2. \quad (1)$$

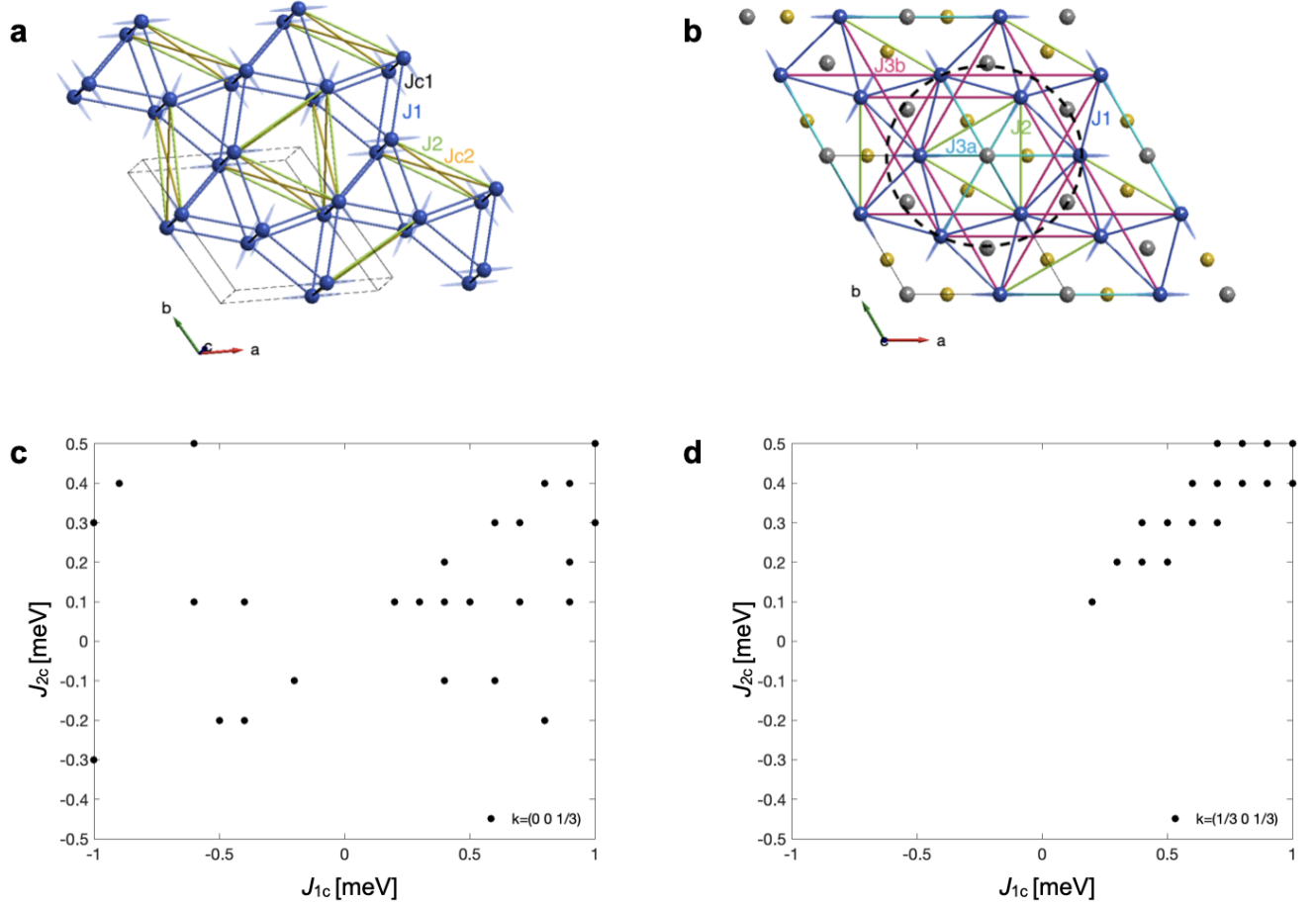
The first term corresponds to the exchange couplings J_{ij} between spins \mathbf{S} on sites i and j of the distorted Kagome plane. The second term pertains the exchanges with components along the c -axis, J_{cij} , and the last term accounts for the magnetic anisotropy A .

Our experimental findings and CEF considerations suggest that the energy scale of the magnetic anisotropy and exchange couplings are of the same order in YbAgGe. Thus, the anisotropy does not dominate the selection of the ordering vector. We fixed the parameter to $A = -1$. Another important experimental fact is that the $q_z = 1/3$ component of the ordering vector is remarkably persistent in all reported ordered magnetic phases up to $\mu_0 H = 7$ T²³. This suggests that exchange interactions extending along the c -axis are strong, competing among themselves and with the intraplane couplings.

We minimized the Hamiltonian of Eq.(1) using the SpinW software⁴⁷, restricting the J -parameter space to the nearest neighbours presented in Fig. S2 and scanned the exchanges within $[-1..1]$ intervals using a grid step of 0.05. We recorded the minimal energy solutions with propagation vectors corresponding to the experimentally observed vectors $q_1=(1/3, 0, 1/3)$, its arms and $q = (0, 0, 1/3)$. Firstly, we considered only exchanges up to the second next-nearest neighbours in- and out- the plane, presented in Fig. S2a. The solutions with propagation vectors $q_z = 1/3$ spread over all considered intervals of J_1 , J_2 and J_{c1} , but J_{c2} was confined to $[-0.5..0.5]$ region (Fig. S2c). With this set of couplings the propagation vector $q_1=(1/3, 0, 1/3)$ was not found. Then we included the equidistant but distinct J_{3a} and J_{3b} in-plane couplings (Fig. S2b) into the simulations. The difference between J_{3a} and J_{3b} becomes apparent when inspecting the hexagon encircled by a dashed black line around the $\bar{6}$ -axis (cell origin) in Fig. S2b. The cyan colored J_{3a} bonds pass through the middle of the hexagon, while the pink J_{3b} bonds span its periphery. As the J -parameter space expanded significantly, we used a cruder grid step of 0.3. The solutions with $q_1=(1/3, 0, 1/3)$ were found for finite J_{3a} and J_{3b} values (both positive and negative). Interestingly, these equidistant, but different couplings were decisive already in selecting the magnetic field-induced states in TmAgGe²². For YbAgGe the stabilizing the $q_1=(1/3, 0, 1/3)$ propagation vector requires J_{c1} and J_{c2} to be positive, that is AFM (Fig. S2d).

We then modeled the diffuse scattering observed at $T = 0.72$ and 0.69 K, just above the ordering temperature $T_N = 0.68$ K. The J_{cij} terms were neglected, because the $q_z = 1/3$ correlations are already established at these temperatures. This allows us to concentrate on the distorted Kagome plane. Firstly, we constructed a hypothetical two-dimensional long-range $q = (0, 0)$ structure with 120 deg canted magnetic moments such as presented in (Fig. S3d). The order represents a compromise between the local CEF anisotropy and AFM J_1 and J_2 couplings; the moments connected by the J_{3a} - and J_{3b} - bonds would be parallel within such an arrangement. In reciprocal space the corresponding hk -plane will contain sharp magnetic Bragg peaks at integer positions where $h + k = 2n + 1$. A confinement of the correlations to few unit cells only results in diffuse scattering around these hk positions. The Fourier transform of a box with $3 \times 3 \times N$ unit cells of this order calculated by program Scatty²⁵ (Fig. S3g) qualitatively reproduces the diffuse pattern measured at $T = 0.72$ K (Fig. S3a). We interpret this good match as the evidence of prevalent $q = (0, 0)$ correlations resulting from the local anisotropy and AF J_1 and J_2 couplings, and their extension over up to three unit cells at $T = 0.72$ K. We attempted to reproduce the pattern at $T = 0.69$ K by i) considering parallel moment alignments on the J_{3b} bonds, ii) populating only every third hexagon, as shown in Fig. S3e and iii) limiting the size of coherent spin arrangements. Figure S3h shows the Fourier transform of a box containing $10 \times 10 \times N$ unit cells, confirming the success of this approach. The model captures the main features of the measured $T = 0.69$ K pattern, *i.e.* the intensity at the main hk positions and the smeared satellites at $q = (1/3, 0)$ and its equivalents.

At $T = 0.25$ K the ordering vector $q=(1/3, 0, 1/3)$ and its arms supersede any remains of the $q = (0, 0)$ structure (see Fig. S3c). The intensity at the main hk positions vanishes, leaving only satellite peaks. We can reproduce the diffraction pattern (see Fig. S3i) by Fourier transforming a $24 \times 24 \times N$ box containing three domains with the $q_1=(1/3, 0)$, $q_2=(0, 1/3)$, $q_3=(-1/3, 1/3)$ propagation vectors and the amplitude modulated arrangement proposed in Ref. ²³. In this model the moment alignments connected by J_{3a} and J_{3b} alternate between parallel and antiparallel, as shown in Fig. S3f. The transformation of magnetic arrangement suggests that the long-range q_1 magnetic order in YbAgGe is established as a compromise between the CEF anisotropy, AFM J_1 and J_2 couplings and competing AFM J_{3a} and J_{3b} couplings.

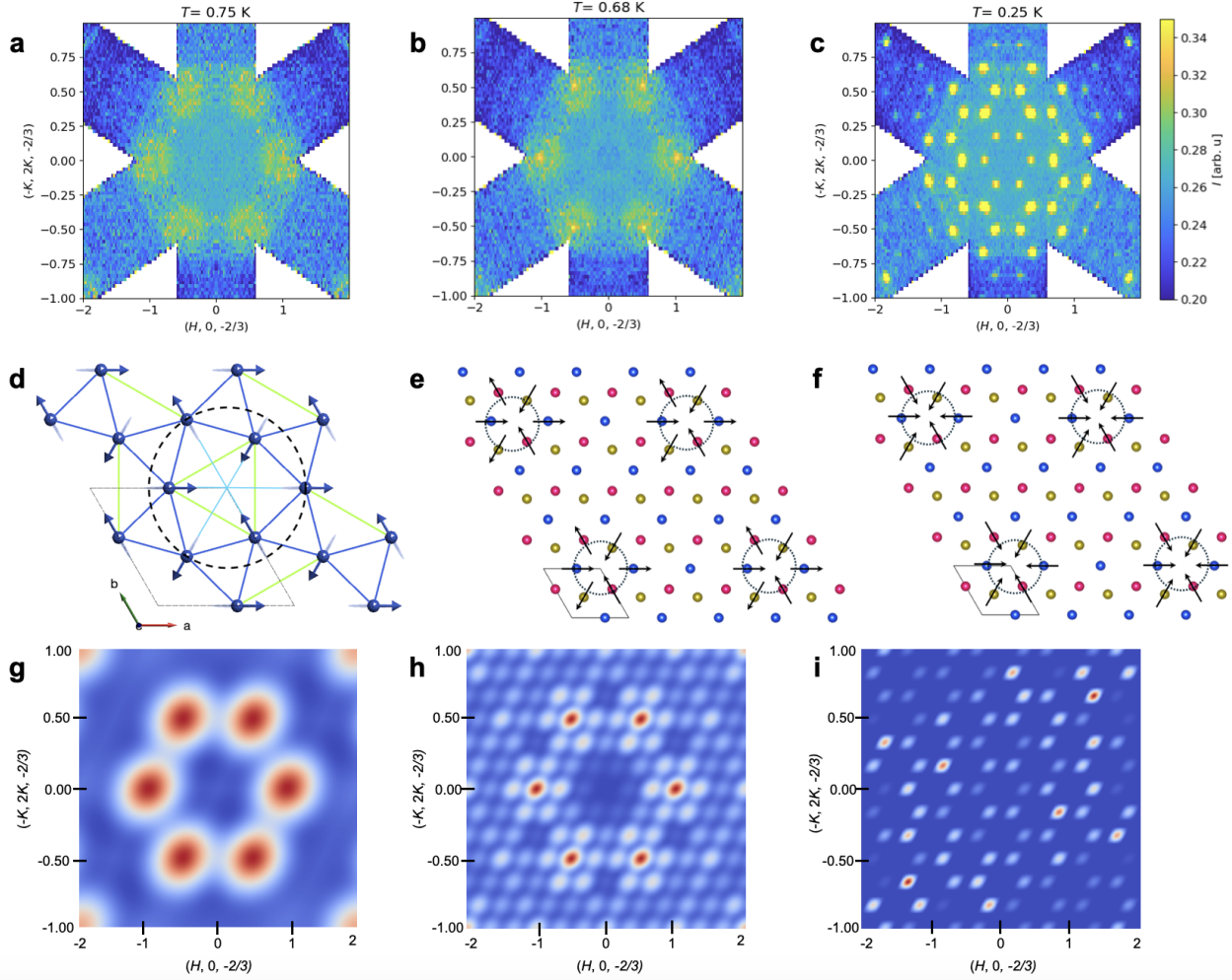


Supplemental Figure 2. Exchange couplings and results of local Hamiltonian minimization. **a** Nearest neighbour exchange couplings J_1 (blue), J_2 (green) in-plane and J_{c1} (black), J_{c2} (gold) out-of-plane alongside with the single-ion anisotropy (blue ellipses). **b** in-plane J_1 , J_2 , J_{3a} (cyan) and J_{3b} (pink) couplings. Yb, Ge and Ag atoms are colored in blue, gray and gold, respectively. The dashed black circle spans over a hexagon of edge sharing Yb-triangles, the elemental building block of the geometrical Yb^{3+} building block. **c** Distribution of the lowest energy solutions with magnetic ordering vectors $q = (0, 0, 1/3)$ and **d** $q_1 = (1/3, 0, 1/3)$ as a function of J_{c1} and J_{c2} . The other couplings, J_1 , J_2 , J_{c1} vary within $[-1 \dots 1]$ intervals, J_{c2} within $[-0.5 \dots 0.5]$.

SUPPLEMENTARY NOTE 4: STATIC CORRELATIONS

The temperature dependence of the magnetic correlation lengths was determined by one dimensional (1D) line-cuts through the data presented in Fig. 2 of the main manuscript. The four-dimensional dataset measured on CNCS with $E_i = 12$ meV was integrated over $\Delta E = \pm 0.25$ meV around the elastic line and $\Delta Q = \pm 0.05$ reciprocal lattice units (rlu) perpendicular to the cutting direction. In Fig. S4a we show 1D-cuts along $(\langle H \rangle, 0, L)$ with $\langle H \rangle = 0$ and $1/3$ for temperatures above and below $T = 0.68$ K, respectively. Panel b displays cuts along $(H, -1, -2/3)$. The resulting 1D-cuts were fitted by Gaussian line shapes, from which the correlation lengths $\xi_c = c/\pi\text{FWHM}$ and $\xi_a = a/\pi\text{FWHM}$ were determined as function of temperature. FWHM denotes the full-width at half-maximum of the Gaussian peaks.

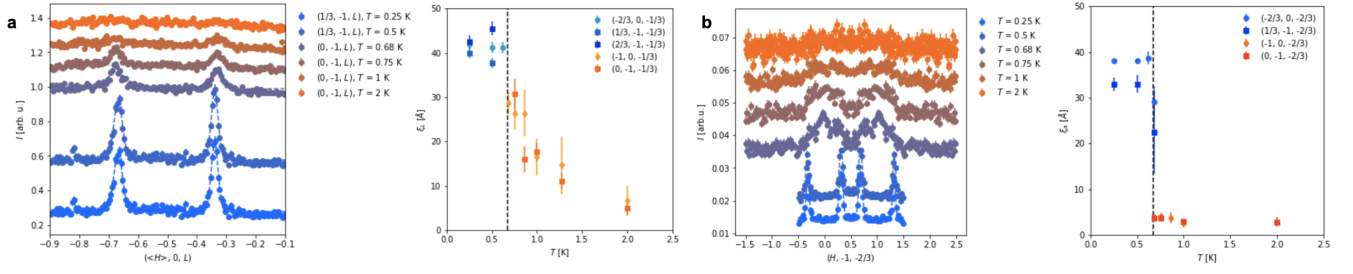
The temperature dependence of the correlation lengths ξ_c and ξ_a shows that at $T = 2$ K the material is correlated over ~ 5 Å along the c -direction, and ~ 4 Å along the a direction. Upon cooling $\xi_c(T)$ is continuously increasing and reaches the resolution limited correlation of structural Bragg peaks (~ 10 unit cells) below $T = 0.68$ K. This behavior is different for $\xi_a(T)$, where the correlation length remains unchanged above $T > 0.68$ K. A discontinuous jump of $\xi_a(T)$ is observed at $T = 0.68$ K below which the correlation length reaches 5 unit cells which match the correlation length of structural Bragg peaks.



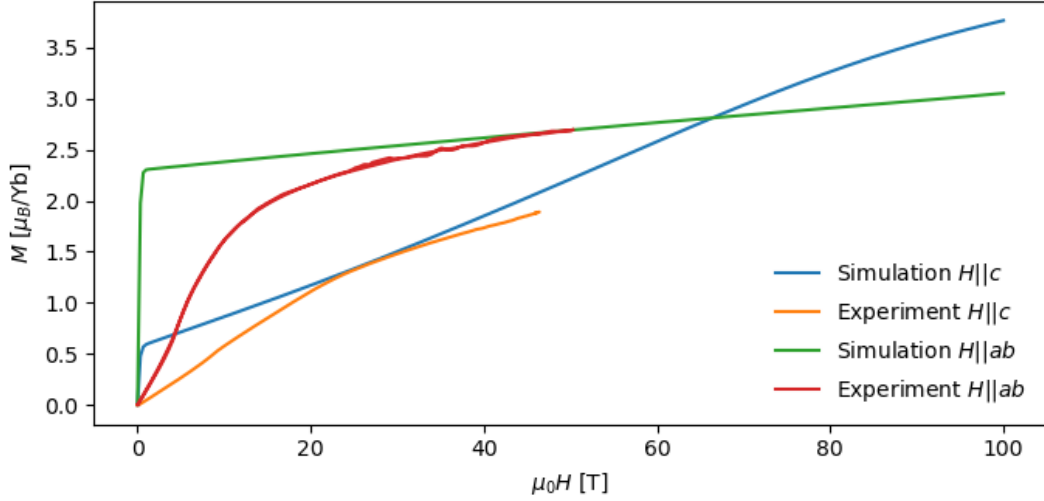
Supplemental Figure 3. Diffuse scattering in experiment and simulation. Experimental $(H, K, 1/3)$ cuts through the CNCS data at $T = 0.72$ K **a**, 0.69 K **b** and 0.5 K **c**. **d** The magnetic moment arrangement within the hypothetical $q = (0, 0)$ structure, a dashed black circle spans over a Yb-hexagon. **e** The $3a^* - 3b^*$ structure with the parallel moment alignment connected by J_{3a} . **f** The $3a^* - 3b^*$ structure with the antiparallel moment alignments. Calculated (H, K) cuts simulated via Fourier transform of **g** a $3 \times 3 \times N$ box containing the hypothetical $q = (0, 0)$ structure, **h** a $10 \times 10 \times N$ box with the parallel moment alignment connected by J_{3a} , **i** a $24 \times 24 \times N$ box containing three 120° rotated domains of the zero-field $q_1 = (1/3, 0, 1/3)$ amplitude modulated structure²³ with parallel and antiparallel moment alignments connected by J_{3a} .

SUPPLEMENTARY NOTE 5: HIGH FIELD MAGNETIZATION AND COMPARISON TO CALCULATIONS

The localization degree of the Yb moments was examined through magnetization experiments in pulsed magnetic fields up to $\mu_0 H = 50$ T at the Dresden High Magnetic Field Laboratory, which were normalised to laboratory measurements up to $\mu_0 H = 14$ T reported in Ref.²⁶. Figure S5 depicts the experimental results measured at $T = 0.53$ K on a single crystal for $H \parallel ab$ (red line) and $H \parallel c$ (orange line), respectively. Overplotted in green and blue are the calculated magnetization curves expected from the CEF scheme. We assign the deviations at low magnetic fields to contributions of the magnetic exchange interactions that were not considered in the calculations. For $H \parallel ab$ we find qualitative agreement in the overall field dependence and quantitative agreement at large magnetic fields. In contrast, qualitative deviations occur for $H \parallel c$ above $\mu_0 H \approx 30$ T. For $H \parallel c$ we find that the crystal was misaligned by $\sim 12^\circ$ away from the c -axis due to manual alignment of the small crystal in the ^3He insert. This misalignment is not relevant for the conclusion that the local moment model cannot account for the experimentally observed magnetization curve.



Supplemental Figure 4. Correlation length from short-range correlations. One dimensional line cuts and quantitative analysis of the short-range correlations in YbAgGe along the crystallographic c - and a -direction in **a** and **b**, respectively. The four dimensional data was integrated over $\Delta E = \pm 0.25$ meV around the elastic line and $\Delta Q = \pm 0.05$ rlu perpendicular to the shown cutting direction. The cuts are offset for clarity. The resulting one dimensional line-cuts were fitted by Gaussian line shapes, from which the correlation lengths $\xi_c = c/\pi\text{FWHM}$ and $\xi_a = a/\pi\text{FWHM}$ were determined as function of temperature. FWHM denotes the full-width at half-maximum of the Gaussian peaks.

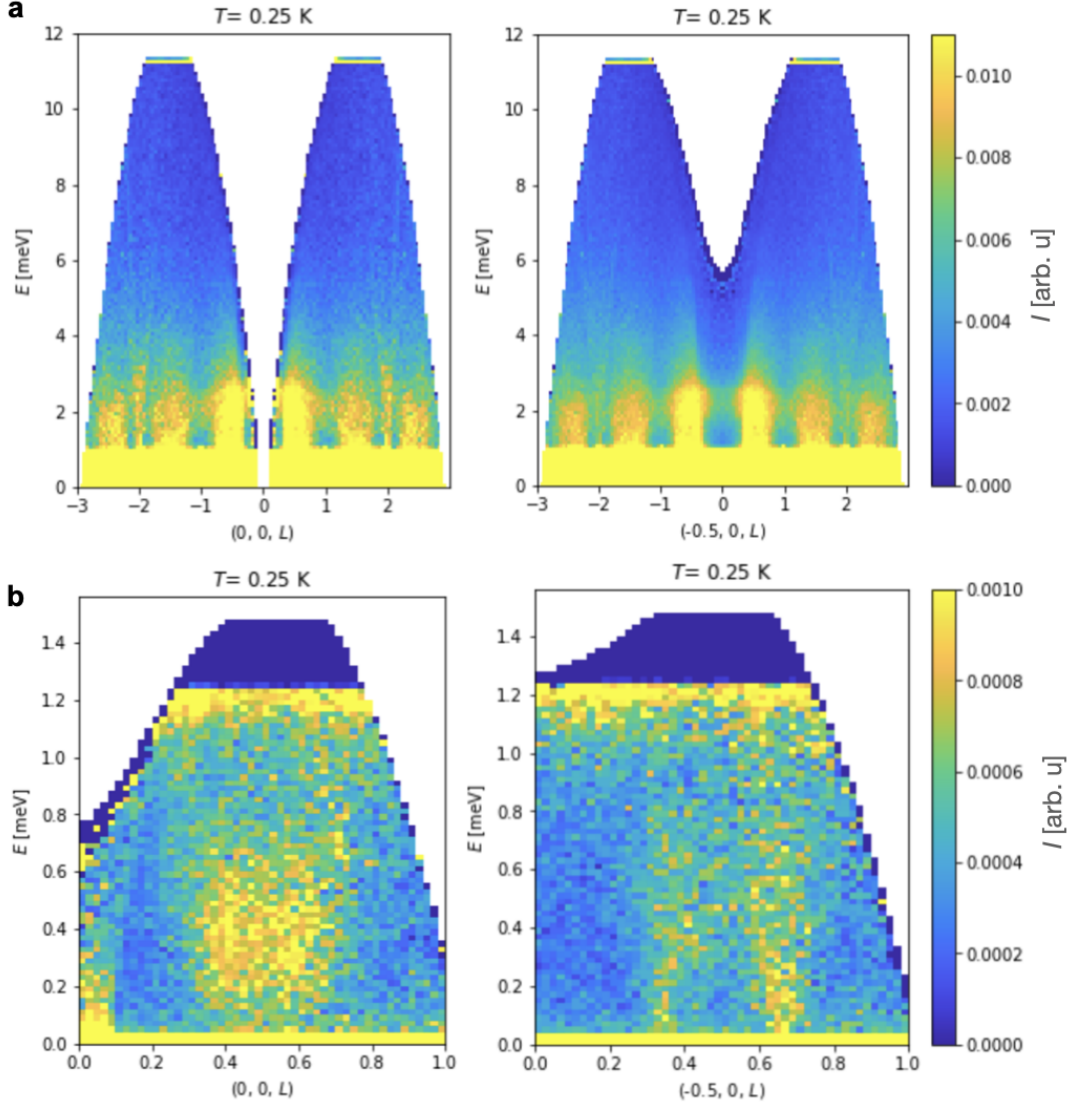


Supplemental Figure 5. High-field magnetization. Field dependent magnetization of YbAgGe for $H||ab$ and $H||c$. The red and orange curves are measurements at $T = 0.53$ K. In green and blue we show the field dependence expected from the crystal-electric field scheme.

SUPPLEMENTARY NOTE 6: DYNAMIC MAGNETISM IN YBAGGE AT ZERO MAGNETIC FIELD

The static and dynamic properties at $\mu_0H = 0$ T and $T = 0.25 - 30$ K were studied on CNCS using incident energies $E_i = 12, 3.32$ and 1.55 meV with elastic energy resolutions $\Delta E = 1.2, 0.175$ and 0.04 meV FWHM. While we show the $E_i = 3.32$ meV dataset at $T = 0.25$ K in Fig. 3 of the main manuscript, the $E_i = 12$ and 1.55 meV datasets along $(0, 0, L)$ and $(-1/2, 0, L)$ are shown in Fig. S6a and b, respectively. The $E_i = 12$ meV dataset provides evidence that the column like excitations at $(H, 0, 1/3)$, $(H, 0, 2/3)$ and $(0, 0, 1/2)$ are the only observable magnetic excitations below the first CEF transition at an energy transfer $E = 12$ meV. The additional cone-like signal around $(0, 0, 2)$ is an acoustic phonon. The high-resolution setting at $E_i = 1.55$ meV reveals no clear excitation gap at low energy transfer. This is further supported by the one-dimensional energy cuts various reciprocal lattice positions shown in Fig. S7a, suggesting that the excitations are quasielastic and do not condense into the ground state.

Following reported inelastic neutron scattering experiments at specific $(H, 0, 1/3)$ and $(1/3, 0, L)$ positions²⁷, we fitted the dynamic susceptibility to a quasielastic Lorentzian $\chi''(q, E) = (E\chi'_q\Gamma_q)/(E^2 + \Gamma_q^2)$. $\chi''(q, E)$ is directly probed by neutron scattering, χ'_q is the real part of the static susceptibility at the wavevector q , and Γ_q is a characteristic energy scale. The results are shown in Fig. S7b,c. We find a wavevector dependent Γ_q that is smallest at $q = (0, 0, 1/2)$ ($0.23(7)$ meV), $0.41(6)$ meV at $q = (0, 0, 1/3)$ and $0.54(7)$ meV in average. Their finite values attest that no quantum critical fluctuations are obscuring the magnetic excitation spectrum at $\mu_0H = 0$ T. Upon increasing temperature the quasielastic Lorentzian fit shows that the wavevector dependence of the static susceptibility χ'_q is

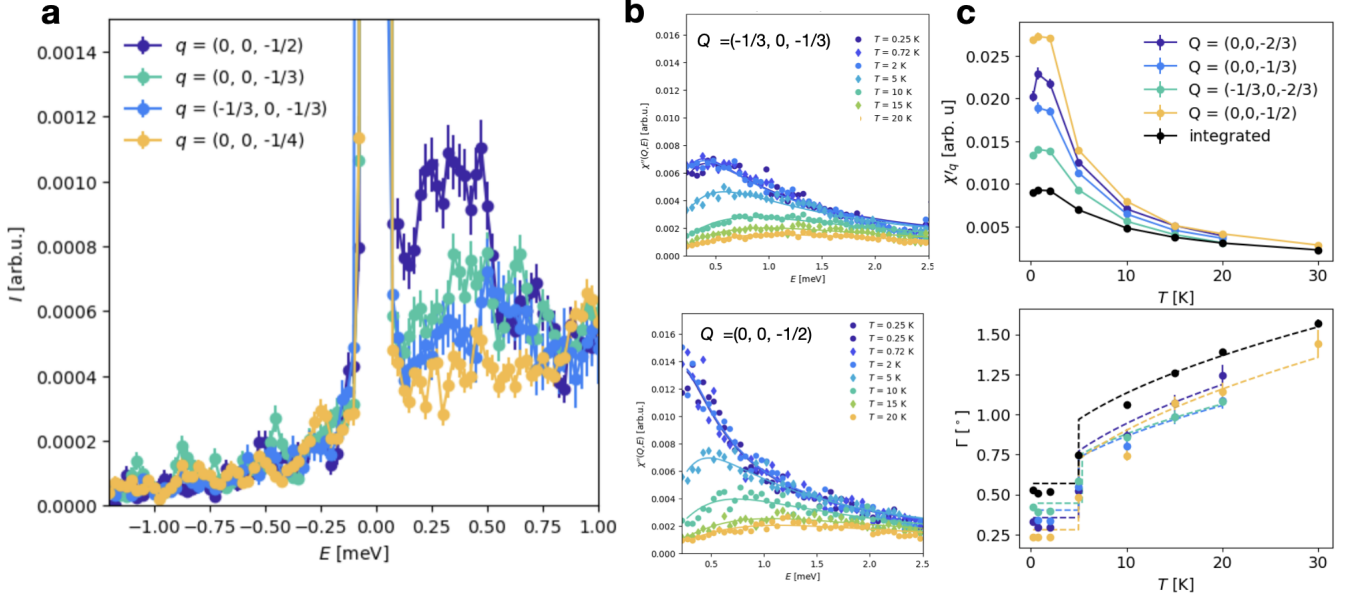


Supplemental Figure 6. Magnetic excitations at $\mu_0 H = 0$ T. Magnetic excitation spectrum of YbAgGe along $(0, 0, L)$ and $(-1/2, 0, L)$ measured at $T = 0.25$ K and $E_i = 12$ and 1.55 meV in **a** and **b**, respectively. We used a reciprocal space integration range $\Delta Q = [-0.2, 0.2]$ perpendicular to the cutting direction.

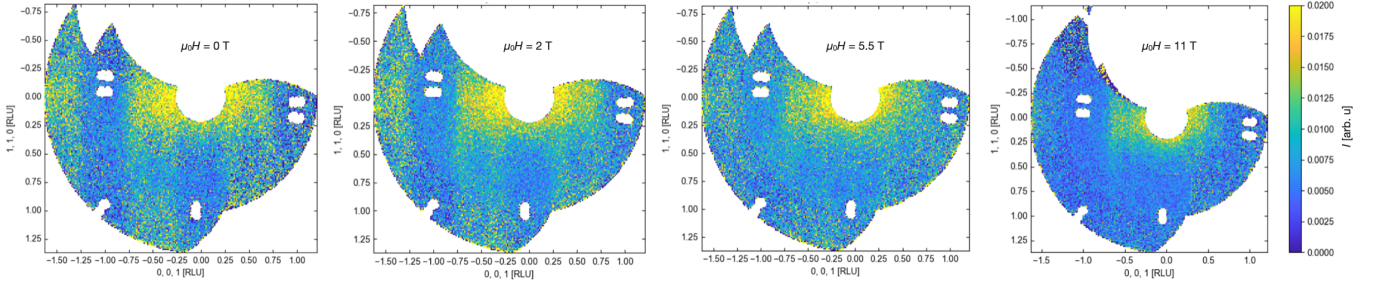
suppressed above T^* . The characteristic energy scale follows the dependence $\Gamma_q(T) = \Gamma_q(0) + \Theta(T - T_s)A\sqrt{T}$ with $A = 0.19(2)$ meVK $^{-1/2}$, and $T_s \approx 5$ K occurring in the step function Θ is close to where χ'_q is maximal.

SUPPLEMENTARY NOTE 7: MAGNETIC FIELD DEPENDENCE OF THE DYNAMIC PROPERTIES

The magnetic field dependent excitations were measured on the cold neutron multiplexing spectrometer CAMEA. In Fig. S8 we show reciprocal space maps of the (H, H, L) plane at an energy transfer $E = 0.6(1)$ meV at $\mu_0 H = 0, 2, 5.5, 11$ T. The data were measured with an incident energy $E_i = 5$ meV. The zero field measurements confirm the column-like excitations with spectral weight along $(H, 0, 1/3)$, $(H, 0, 2/3)$ and around $(0, 0, 1/2)$ observed on CNCS. Apart of a decrease of the neutron intensity the excitations remain unchanged until $\mu_0 H = 5.5$ T under a magnetic field along $H \parallel [1-10]$, despite various changes in the magnetic long-range order²³. At $\mu_0 H = 11$ T we find a broad dispersion along $(0, 0, L)$ that is quasielastic at $(0, 0, 1/3)$ and $(0, 0, 2/3)$ and maximal at $(0, 0, 1)$ with an energy transfer $E = 4$ meV (see Fig. 4 of the main manuscript).



Supplemental Figure 7. Temperature dependence of the dynamic fluctuations. **a** One dimensional line cuts through various reciprocal lattice positions at $T = 0.25$ K using $E_i = 1.55$ meV with an integration of $\Delta Q = [-0.05, 0.05]$. **b** One dimensional line cuts through $q = (0, 0, -1/2)$ and $(-1/3, 0, -1/3)$ as function of temperature using $E_i = 3.32$ meV with an integration range of $\Delta Q = [-0.05, 0.05]$ around the reciprocal lattice positions. Overplotted (dashed lines) are fitted quasielastic Lorentzian lineshapes $\chi''(q, E) = (E\chi'_q\Gamma_q)/(E^2 + \Gamma_q^2)$. $\chi''(q, E)$ is the imaginary part of the dynamic susceptibility directly revealed by neutron scattering, χ'_q is real part of the static susceptibility at the wavevector q , and Γ_q is a characteristic energy scale. The temperature dependence of χ'_q and Γ_q for different q s are shown in **c**. The characteristic energy scale follows the dependence $\Gamma_q(T) = \Gamma_q(0) + \Theta(T - T_s)A\sqrt{T}$ with $A = 0.19(2)$ meV K $^{-1/2}$, and $T_s \approx 5$ K occurring in the step function Θ is close to where χ'_q is maximal.



Supplemental Figure 8. Field dependence of excitations. Reciprocal space maps of the (H, H, L) plane at an energy transfer $E = 0.6$ meV at $\mu_0 H = 0, 2, 5.5, 11$ T along $H \parallel [1-10]$. The data were measured with $E_i = 5$ meV using an energy integration range $\Delta E = [0.5, 0.7]$ meV.

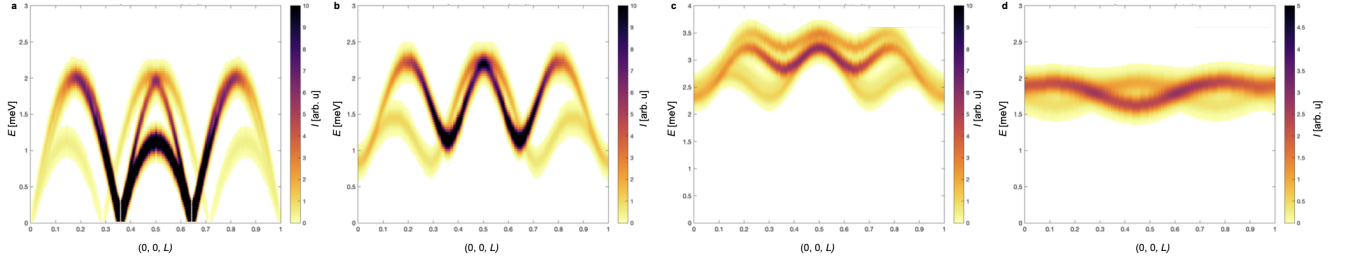
SUPPLEMENTARY NOTE 8: LINEAR SPIN-WAVE SIMULATIONS

We attempted to model the magnetic excitation spectrum of YbAgGe using the local-moment Hamiltonian

$$H = \sum_{ij} J_{cij} \mathbf{S}_i \cdot \mathbf{S}_j + A \sum_i \mathbf{S}_i^2 - g\mu_B \mu_0 \mathbf{H} \sum_i \mathbf{S}_i. \quad (2)$$

The first term describes the exchange couplings along the c -axis between spins \mathbf{S} on sites i and j with exchange couplings J_{cij} . The second term accounts for the anisotropy A , and the last term is the Zeeman term with $H \parallel [1, -1, 0]$. We assumed independent chains along the c -axis with two nearest-neighbour interactions J_{c1} , and J_{c2} , whose ratio leads to a magnetic structure with a propagation vector retaining the $q_z \approx \frac{1}{3}$ periodicity. The values were adjusted

such that a spin-wave boundary of $E \sim 3.5$ meV was obtained at $\mu_0 H = 11$ T, in accordance to the experimental data (see Fig. 4 of the main manuscript).



Supplemental Figure 9. Linear spin-wave simulation. Simulation of the magnetic excitation spectrum along $(0, 0, L)$ using a one dimensional Heisenberg chain without local anisotropy in **a**, with a small axial anisotropy in **b**, and under magnetic field along $H \parallel [1, -1, 0]$ in **c**. Subpanel **d** shows a simulation of a xxz -chain, in which the crystal-field anisotropy was incorporated via anisotropic exchange interactions.

Figure S9a shows the spin-wave dispersion along $(0, 0, L)$ for the Heisenberg chain with antiferromagnetic interactions $J_{c1} = 1.5$ meV, $J_{c2} = 0.6$ meV and $A = 0$ at zero magnetic field. The configurations yield a spiral structure with magnetic Goldstone modes within $E = 0 - 2$ meV. Both, the finite axial anisotropy $A < 0$ mimicking the crystal field anisotropy and non-zero magnetic field lead to a gaped excitation spectrum, as shown in Figures S9b, c for $A = -0.1$ meV and $\mu_0 H = 11$ T, respectively. This contrasts the experimental observations, which report soft excitations up to $\mu_0 H = 11$ T. Thus, we concluded that a one-dimensional Heisenberg chain does not provide a satisfactory description of the observed magnetic excitation spectrum. In an alternative approach we incorporated the crystal-field anisotropy via anisotropic exchange interactions using the effective Hamiltonian

$$H = \sum_{ij} J_{cij}^{xx} S_i^x \cdot S_j^x + J_{cij}^{yy} S_i^y \cdot S_j^y + J_{cij}^{zz} S_i^z \cdot S_j^z \quad (3)$$

with $J_{c1}^{xx} = J_{c1}^{yy} = 0.2$, $J_{c1}^{zz} = 1.5$, $J_{c2}^{xx} = J_{c2}^{yy} = 0$ and $J_{c2}^{zz} = 0.6$ meV. The model yields a magnetic structure with $q_z \approx \frac{1}{3}$. The resulting spin waves are displayed in Fig. S9d, which is also inconsistent with the experimental observations.